Smart Structures and Systems, *Vol. 14, No. 5 (2014) 883-900*
DOI: http://dx.doi.org/10.12989/sss.2014.14.5.883

Testing and modelling of shape memory alloy plates for energy dissipators

Pablo Heresi[a], Ricardo A. Herrera* and Maria O. Moroni[b]

Department of Civil Engineering, Universidad de Chile, Blanco Encalada 2002, 8370449 Santiago, Chile

(Received June 12, 2013, Revised September 20, 2013, Accepted December 22, 2013)

Abstract. Shape memory alloys (SMA) can dissipate energy through hysteresis cycles without significant residual deformation. This paper describes the fabrication and testing of copper-based SMA hourglass-shaped plates for use in energy dissipation devices and the development of a numerical model to reproduce the experiments. The plates were tested under cyclic flexural deformations, showing stable hysteresis cycles without strength degradation. A detailed nonlinear numerical model was developed and validated with the experimental data, using as input the constitutive relationship for the material determined from cyclic tests of material coupons under tension loading. The model adequately reproduces the experimental results. The study is focused on the exploitation of SMA in the martensite phase.

Keywords: shape memory alloy; CuZnAl; seismic dissipation devices; experimental work; numerical modelling

1. Introduction

The use of supplemental energy dissipation for seismic protection or performance enhancement of civil structures has become increasingly popular over the last years. Different types of energy dissipation systems have been developed by a number of researchers and implementations of some of these systems in real structures have rapidly increased around the world. An effective mechanism of energy dissipation consists of inducing inelastic deformations to a metallic element (Symans *et al*. 2008). Among the devices that use this mechanism, there is one type designed to induce bending on hourglass-shaped plates in order to spread the yielding almost uniformly throughout the material, often mild steel. Over the last 20 years this type of plates have been widely investigated and implemented in buildings on seismic areas (Alonso 1989, Tena-Colunga 1997, De la Llera *et al*. 2004). An important issue of this type of devices is that after an earthquake they usually have sustained large inelastic deformations and present significant residual deformations, which leads to the need of replacement.

On the other hand, Shape Memory Alloys (SMAs) are a class of materials which can dissipate energy through hysteresis cycles without significant residual deformation. This is the result of

---

*Corresponding author, Assistant professor, E-mail: riherrer@ing.uchile.cl

[a] M.Sc., E-mail: pabloheresi@gmail.com

[b] Associate professor, E-mail: mmoroni@ing.uchile.cl

http://www.techno-press.org/?journal=sss&subpage=8 ISSN: 1738-1584 (Print), 1738-1991 (Online)

reversible phase transformations of the material between Austenite and Martensite, under temperature or stress changes. Four temperatures define the phase transformation limits at the unstressed state: start martensite (M_S) and finish martensite (M_f), when the material is cooled from Austenite phase, and start austenite (A_S), and finish austenite (A_f), when the material is heated from Martensite phase. The behavior under load depends on the initial phase of the material: if the initial phase is Austenite, the alloy may present the Superelastic Effect (SE), which exhibits a characteristic flag-shaped hysteretic cycle, recovering its original shape after removal of the load while dissipating energy; if the initial phase is Martensite, the alloy shows the Shape Memory Effect (SME), where the hysteretic cycle ends with residual deformations which can be recovered after heating the material above A_f and letting it cool below M_f. McCormick (2006) describes the characteristic hysteresis loops for both phenomena. These self-centering and energy dissipating characteristics make SMAs a promising material for seismic protection.

An extensively used SMA is Nitinol, made of Ni and Ti, which has found application in medicine and aeronautics. The use of this alloy in a wide range of seismic applications has also been investigated: Nitinol devices have been included as braces in steel frames (Asgarian and Moradi 2011, Miller *et al.* 2012), as connectors in beam-column joints of steel frames (Speicher *et al.* 2011) or as reinforcement in beam-column joints of reinforced concrete frames (Youseff *et al.* 2007, Alam *et al.* 2012, Abdulridha *et al.* 2013). Recently, the inclusion of SMA devices in bridges has been reported by several authors (Johnson *et al.* 2008, Dong *et al.* 2011, Torra *et al.* 2013, Bhuiyan and Alam 2013, Dieng *et al.* 2013).

Some copper based SMAs have also been developed, but commercial fabrication has been restricted to small diameter wires and bars. The most available alloy is CuAlBe. Research on copper based SMAs has been mainly focused on the characterization of thermo-mechanical properties. It has been found that thermal treatment, aging process, grain size and sample size are key parameters that determine the SMA behavior (Casciati and Van der Eijk 2008, Montecinos *et al.* 2008). Tension tests of copper based SMA samples (Sutou *et al.* 2005, Somerday *et al.* 1997) show that the grain size significantly affects the post "yielding" (start of phase transformation or detwinning process) slope of the stress-strain curve, whereby increasing the grain size decreases this slope. However, the elastic modulus of the material does not change significantly with a change in the grain size. On the other hand, the duration of the thermal treatment affects the fracture life of the SMAs. Excessive grain growth, generated by a longer thermal treatment, produces a more brittle material, resulting in an earlier failure. Carreras *et al.* (2011) and Casciati and Marzi (2010) studied the fatigue life of austenitic NiTinol and CuAlBe SMA bars and concluded that both materials can withstand over a 1000 cycles of deformation, which they established as a reasonable number of cycles to represent a seismic input.

Several analytical models with varied degrees of complexity have been developed to capture the constitutive law of SMAs. Motahari and Ghassemieh (2007) proposed a multilinear curve to represent the stress-strain relationship, which simulates various complex behaviors of SMAs, such as superelastic effect, partial superelastic effect, detwinning, and high rate loading (under adiabatic conditions). This model stands out because of its simplicity and versatility.

This paper reports the findings of research on copper based SMA hourglass-shaped plates for use in energy dissipation devices. These plates were fabricated and tested under cyclic flexural deformations with different amplitudes. In addition, material coupons were tested under tension loading to obtain the constitutive law of the material. The experimental data was then used to calibrate an analytical stress-strain relationship model. Finally, a detailed non-linear numerical model of an hourglass-shaped plate, suitable for use in complex structural models, was developed and validated against experimental data. The study is focused on the exploitation of SMA in the martensite phase under a low number of cycles.

2. Experimental study

2.1 Preparation of samples

Two 50 kg heats of a CuZnAl alloy (called Heat A and Heat B) were prepared based on the following nominal composition: Cu - 16.90%wt. Zn - 7.71%wt. Al. – 0.04%wt. B. However, the actual compositions of each heat, obtained using optical spectroscopy, are presented in Table 1. The large variation in the Zn proportion is consequence of the use of an open furnace to fabricate the alloy. This makes it difficult to control the amount of Zn lost by evaporation to the atmosphere during the process. The small percentage of B could not be detected in these analyses. The heats were cast in cylindrical molds and each cast was forged to obtain a total of 8 rectangular plates of 150 mm x 300 mm x 15 mm, plates 1 through 3 from Heat A and plates 4 through 8 from Heat B.

A thermo-mechanical treatment was applied to all the plates in order to reduce their thickness approximately to the nominal value for the specimens (8 or 10 mm). Plate-4 was hot-rolled at 700°C, but because of the rapid cooling of the plate, it ended up with a permanent curvature that could not be completely removed. In consideration of this result, the procedure was changed and the rest of the plates were heated up to 850ºC, press-formed to reduce the thickness, and finally quenched with iced water. During this process, Plate-2 fractured in such a way that a specimen could not be extracted from it. A second thermo-mechanical treatment consisted in heating the elements up to 850ºC for 15 minutes, and water quenching them at room temperature. Before applying this second treatment, each remaining plate was machined to obtain a final thickness between 8 and 10.6 mm and an hourglass-shape, as shown in Fig. 1(a). From each plate, a coupon (Fig. 1(b)) to test in tension was also obtained. Then, the thermal treatment was applied to the hourglass-shaped plates and the coupons. Differential Scanning Calorimeter (DSC) analysis and optical metallographies were performed to samples of the plates to establish the phase transformation temperatures M_S, M_f, A_S and A_f, to measure average grain sizes, and to verify the initial phase.

DSC and metallographies showed Martensite phase at room temperature in all the samples, with an average grain size around 0.4 [mm], as shown in Fig. 2. Transformation temperatures of each heat are shown in Table 1. The final sizes of specimens and coupons, as well as the nominal dimensions, are described and listed in Fig. 1 and Tables 2 and 3, respectively.

Table 1 Nominal and actual heat compositions and phase transformation temperatures

Heat	Cu	Zn	Al	Mf	Ms	As	Af
	%wt	%wt	%wt	[ºC]	[ºC]	[ºC]	[ºC]
Nominal	75.35	16.90	7.71	-	-	-	-
A	75.09	17.43	7.48	275	350	280	393
B	78.23	15.40	6.37	278	331	258	384

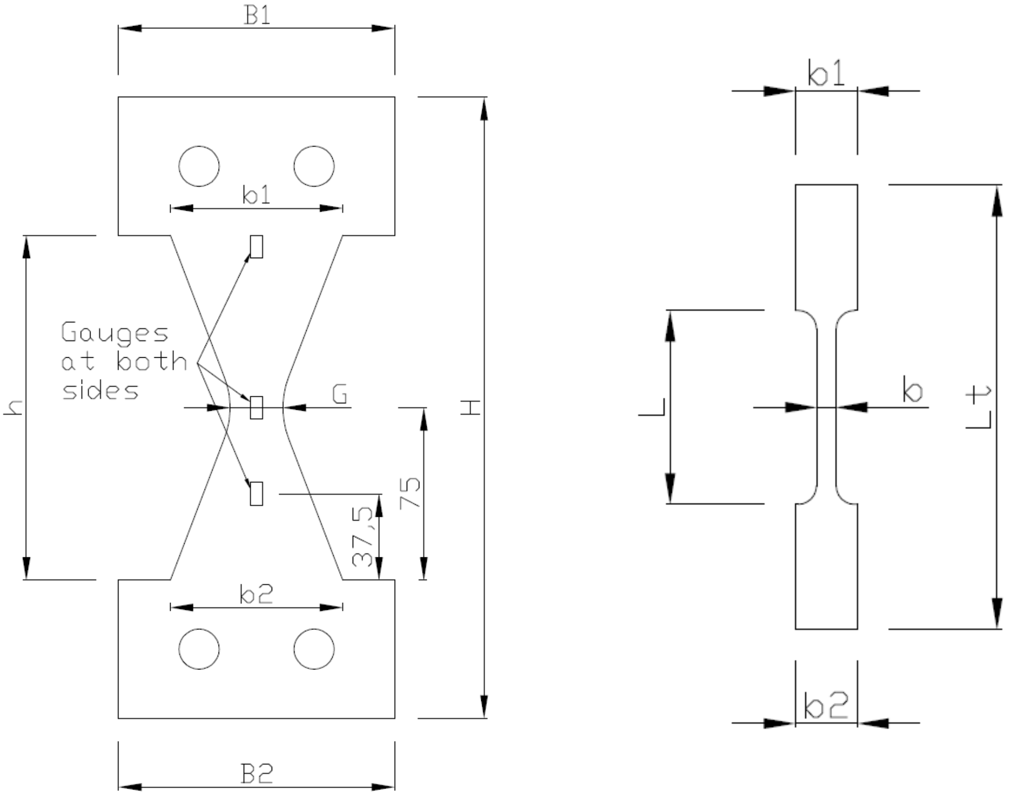

(a) Plate (b) Coupon

Fig. 1 Specimen dimensions in mm

Table 2 Dimensions of hourglass-shaped plates

Plate	B1 [mm]	B2 [mm]	b1 [mm]	b2 [mm]	G [mm]	t1* [mm]	t2* [mm]	tg [mm]	h [mm]	H [mm]
Nominal	120.0	120.0	75.0	75.0	23.0	8 / 10	8 / 10	8 / 10	150.0	270.0
Plate-1	120.5	120.5	76.0	76.0	23.3	8.2	8.0	8.0	149.7	270.0
Plate-2	-	-	-	-	-	-	-	-	-	-
Plate-3	120.1	120.0	76.1	76.0	23.2	10.1	10.1	10.1	150.0	270.0
Plate-4	108.7	108.7	75.7	75.7	23.1	10.6	10.6	10.6	149.7	271.0
Plate-5	120.0	120.3	75.7	75.7	23.1	8.1	8.0	8.0	149.7	271.0
Plate-6	120.2	119.8	76.3	76.6	23.2	10.2	10.1	10.1	149.8	271.0
Plate-7	119.8	120.0	76.7	76.3	23.2	10.1	10.1	10.1	150.1	270.0
Plate-8	120.1	119.9	76.1	76.1	23.1	8.2	8.2	8.2	150.0	270.0

* t1 and t2 are the thicknesses measured at the ends of the plate (where b1 and b2 are measured), and tg is the thickness measured at the center of the plate

Table 3 Dimensions of coupons

Coupon	b1 [mm]	b2 [mm]	b [mm]	L [mm]	Lt [mm]	t* [mm]
Nominal	20.0	20.0	6.3	62.0	142.0	8 / 10
C-1	20.0	20.1	6.3	61.6	142.4	8.1
C-2	-	-	-	-	-	-
C-3	20.0	20.0	6.4	61.8	141.5	10.1
C-4	20.1	20.0	6.3	62.1	142.1	9.4
C-5	20.0	20.0	6.3	62.0	142.2	8.2
C-6	20.0	20.0	6.3	61.9	142.3	10.1
C-7	20.0	20.0	6.4	61.8	142.0	10.1
C-8	20.2	20.1	6.4	61.7	142.2	8.3

* t is the thickness measured at the center of the coupon

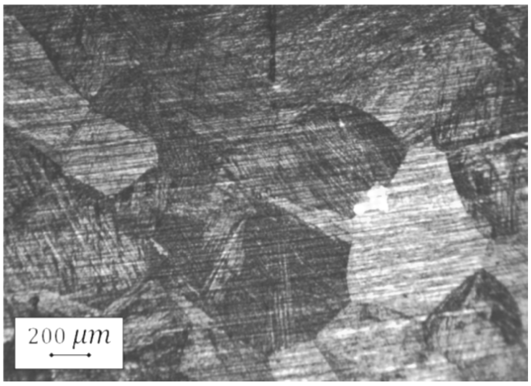

Fig. 2 Sample metallography

2.2 Experimental procedure and results

Flexural tests on the plates and tension tests on the coupons were performed at the Georgia Institute of Technology using an MTS 810 Universal Testing Machine, equipped with MTS 647 Hydraulic Wedge Grips. A 250 kN load cell measured the force, while the grip displacement was measured by an internal LVDT. The actuator was set to run on displacement control for both types of tests; however, for the coupon tests, the control included a routine to avoid generating compression to the samples, based on monitoring the load while unloading the sample and reversing the displacement when the load was within a tolerance of zero. In order to induce bending on the plates, a steel frame was designed and built. Its scheme is shown in Fig. 3. All the tests were performed at room temperature (around 20°C), so all the samples were in martensite phase.

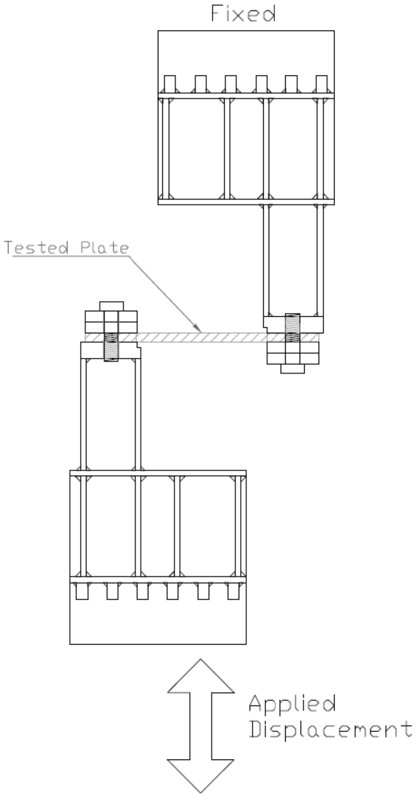

Fig. 3 Test setup

Material coupons were tested under cyclic tensile stresses at two different frequencies: 0.025 and 1 Hz. Data was acquired at a sampling rate of 200 samples per second. For coupons C-1, C-4, C-5 and C-6, the loading sequence consisted of one cycle at 0.5% strain followed by one cycle at 1%, and cycles of increasing amplitude at increments of 1% up to fracture. For coupons C-3, C-7 and C-8, the sequence considered amplitude increments of 0.5% strain. The coupon elongation was estimated from the grip displacement, considering that the compliance of the testing machine accounted for less than 0.1% of this value. Fig. 4 shows the engineering stress-strain curves obtained for both heats at each frequency. The envelope curve is nearly bilinear, with “yield” stresses and strains of about 190 MPa and 0.5% for heat A, respectively, and 220 MPa and 0.7% for heat B. The shape of the curves is characteristic of martensite, and it is similar to that obtained by Gibson (2008), although, transformation limits of both alloys are higher in the present study. Residual deformations in every cycle are significant. No frequency dependence is observed in the stress-strain behavior, for the range of frequencies considered, and heat B shows larger ductility than heat A (on average 5.5 vs. 3.8). On coupons C-7 and C-8, the test was stopped at 3.5% strain to verify the shape memory effect before the coupons fractured. After the coupons were removed from the machine, a thermal treatment was applied to them. The treatment consisted on heating the coupon to 450ºC (above Af), and cooling it back at room temperature. Recoveries of 61% and 39% of the residual deformation were achieved on coupons C-7 and C-8, respectively.

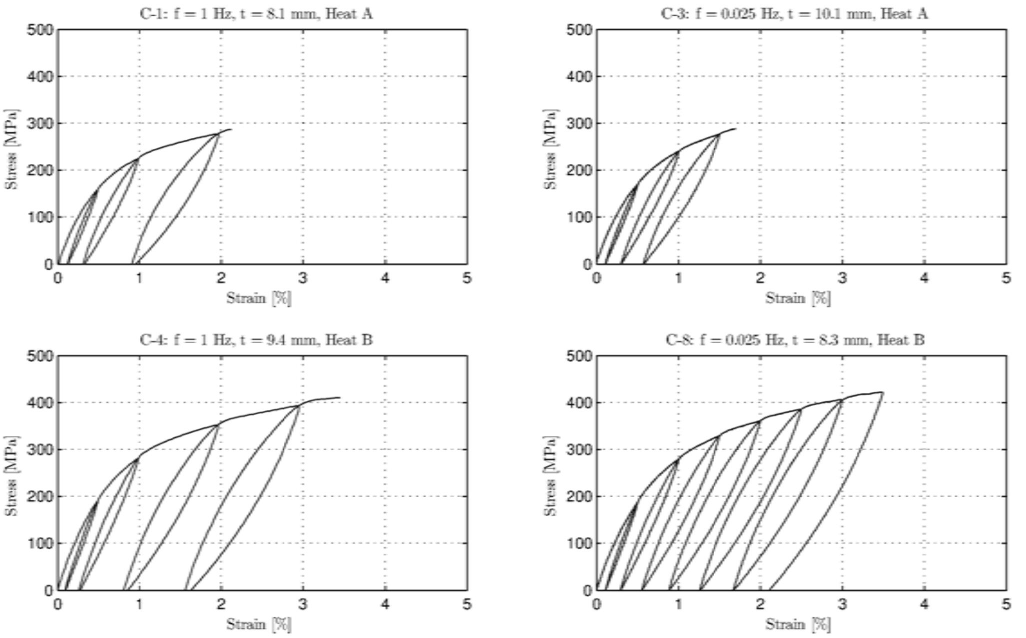

Fig. 4 Stress-strain relationships from tensile coupon test

Cyclic sinusoidal flexural deformations of increasing amplitude at a constant frequency of 0.2 [Hz] were imposed to the plates. The loading sequence applied to each specimen is shown in Fig. 5. In addition to the instrumentation already described, each plate was instrumented with 6 strain gauges as shown in Fig 1(a). The strain gauges were located to try to capture the distribution of curvature and axial deformation along the length of the plate. Data was recorded at 100 samples per second.

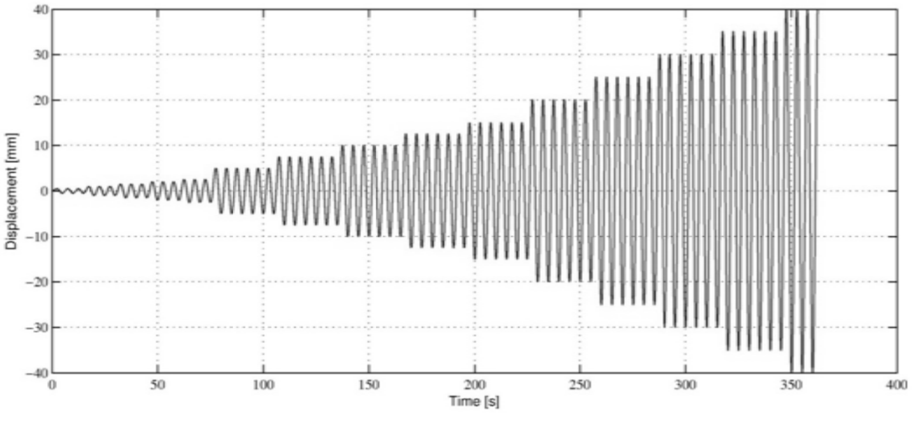

Fig. 5 Loading sequence for plate tests

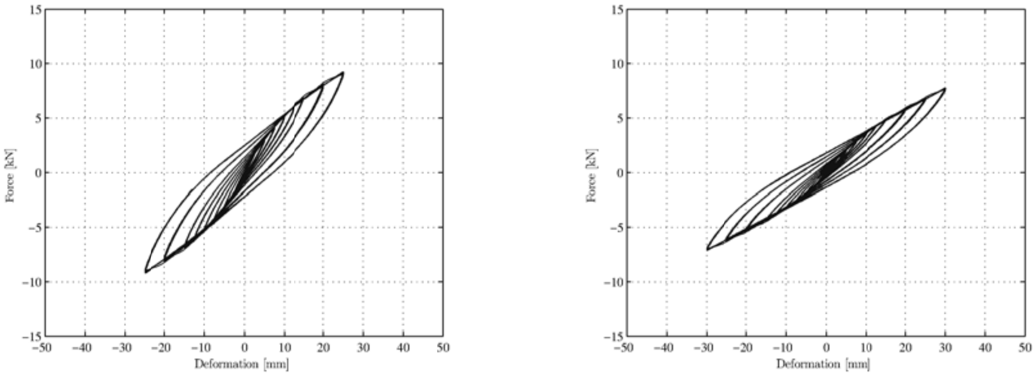

(a) Plate-3: Heat A, t = 10.1[mm] (b) Plate-5: Heat B, t = 8.0[mm]

Fig. 6 Overall Force-Displacement curves

Fig. 6 shows the overall force-displacement curves obtained for one representative specimen of each heat. These results are similar in shape to those obtained by Vargas (2007) for the same type of plates. Fig. 7 shows the deformed shape and the residual deformation after the test of one plate.

Consistent with the results from tensile tests, the heat B plates withstood larger displacements before fracture occurred. The plates present stable and symmetric hysteretic cycles, dissipating energy with no strength degradation; at each imposed displacement, the same force is attained. Figs. 8(a) and 8(b) show the distribution of axial strain, obtained from strain gauge measurements, on the upper and lower fibers. With this data, total axial deformation and curvature were computed assuming a symmetrical deformation pattern (Figs. 8(c) and 8(d), respectively). As could be expected theoretically, for low drift values ($\gamma = d/h$, with d: maximum displacement imposed and h: length of the plate), curvature is nearly constant along the length and total axial deformation is negligible. For higher drift values, the curvature significantly increases at the ends, while some axial deformations are perceptible, indicating the development of membrane action. Strains are shown up to 13.4% drift (displacement amplitude of 20 [mm]) since for larger values, the strain gauges failed (gauge maximum strain was 2%).

(a) Maximum deformation of Plate-5 (b) Residual deformation of Plate-3, after the test

Fig. 7 Maximum deformation and residual deformation of plates

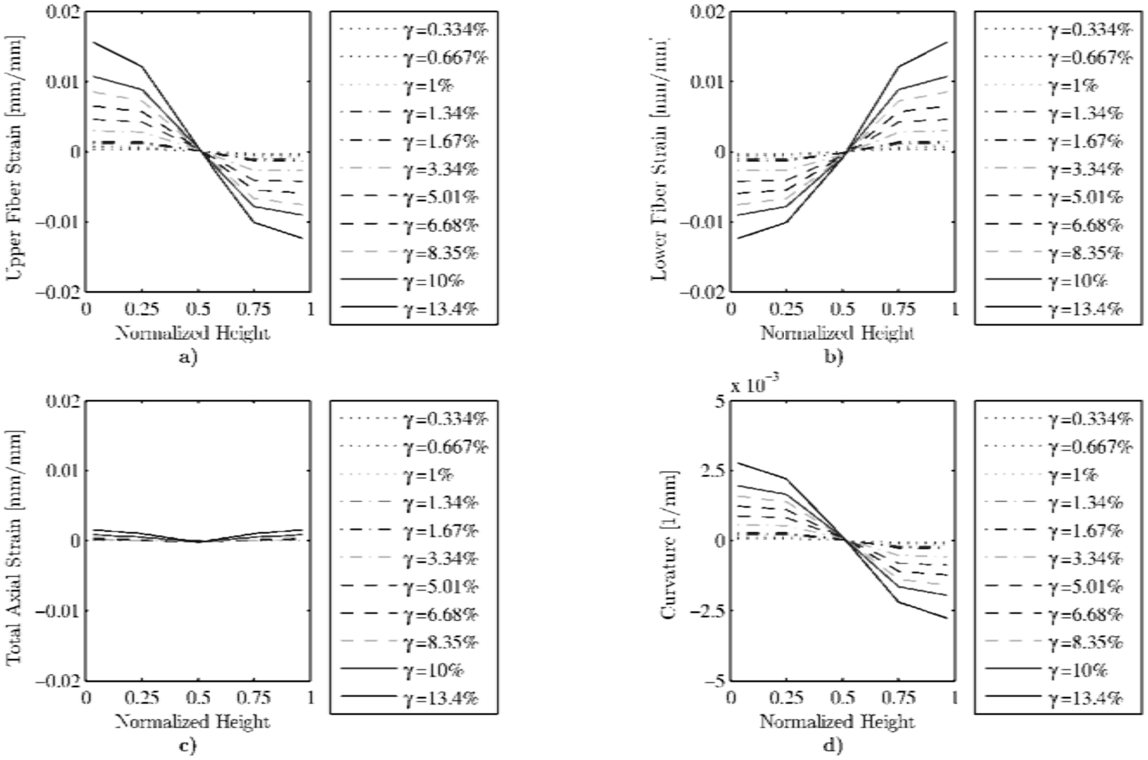

Fig. 8 Strain and Curvature recorded along the plate height. Plate-3, Heat A

For all the plates, Effective Stiffness (Keff), Energy loss (Ed) and Equivalent Viscous Damping Ratio (βeq) were computed on each cycle (Eqs. (1) and (2)).

$$K_{eff} = \frac{|F^{+}| + |F^{-}|}{|d^{+}| + |d^{-}|} \tag{1}$$

$$\beta_{eq} = \frac{E_d}{4\pi \cdot E_s} \tag{2}$$

Where F^{+}, F^{-}, d^{+} and d^{-} are the maximum and minimum force and displacement of each cycle. The energy loss (E_d) corresponds to the total area of the hysteresis cycle, while E_s is the maximum elastic energy of the cycle (½ $K_{eff}(d^{+})^{2}$).

The results from cycles with the same amplitude were averaged, obtaining these results as a function of the displacement amplitude imposed.

Fig. 9 shows the variation of the average normalized effective stiffness (K_{eff} divided by the initial elastic stiffness) with drift (displacement amplitude divided by the length of the plate). The effective stiffness diminishes significantly with the displacement: for 16.6% drift the effective stiffness decreases to 50% of the initial value. The average normalized Energy loss (E_d divided by the plate volume) as a function of drift is shown in Fig. 10. Energy loss significantly increases for larger drifts. The equivalent damping ratio evolution is shown in Fig. 11. It can be seen that it increases with the displacement imposed, reaching values of up to 13% of the critical damping for the larger drift cycles. These values are higher than the ones obtained in past tests of CuZnAl plates (around 8-10%) (Vargas 2007), CuZnAl small diameter bars (around 5-6%) (Gibson 2008), and CuAlBe cables (around 6%) (Beltran *et al*. 2011).

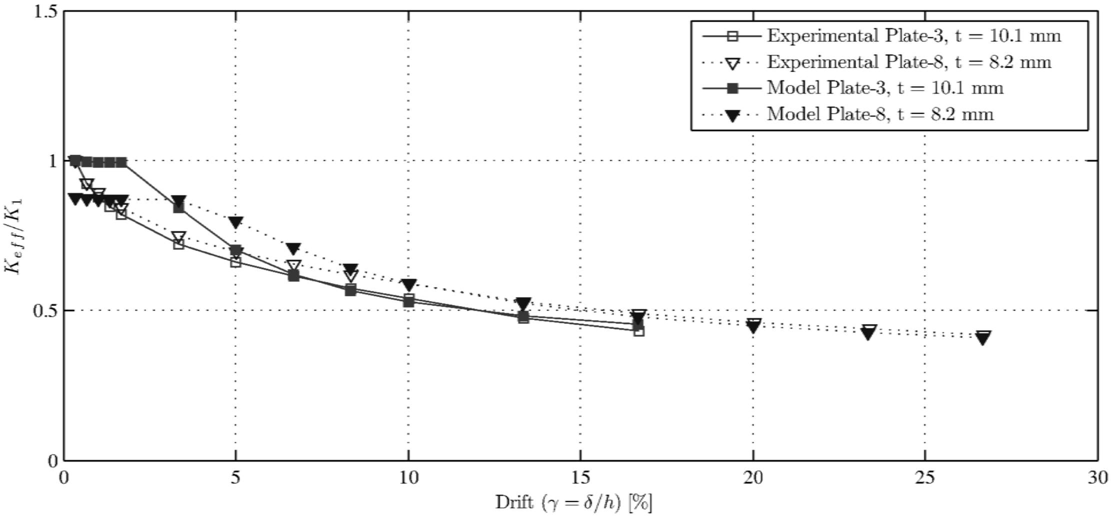

Fig. 9 Normalized effective stiffness as a function of drift

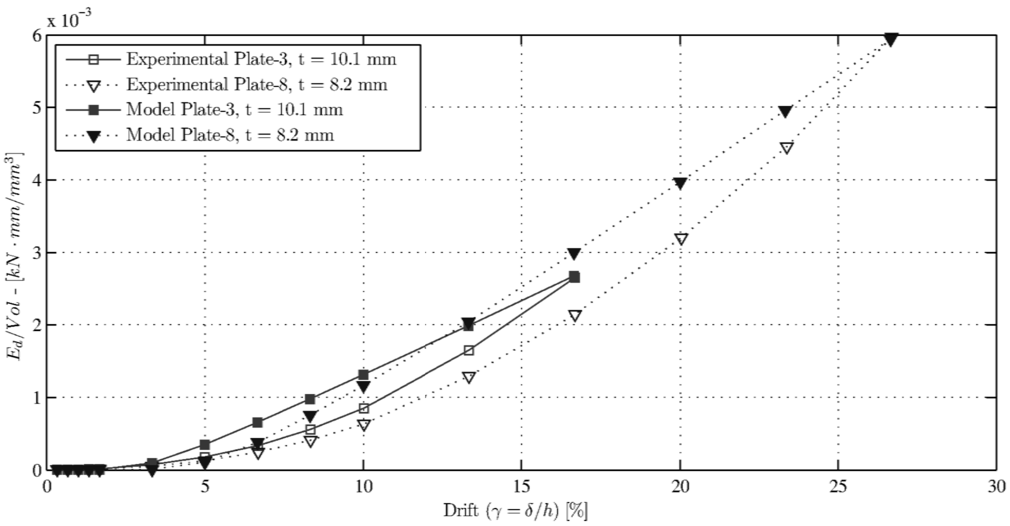

Fig. 10 Normalized energy loss as a function of drift

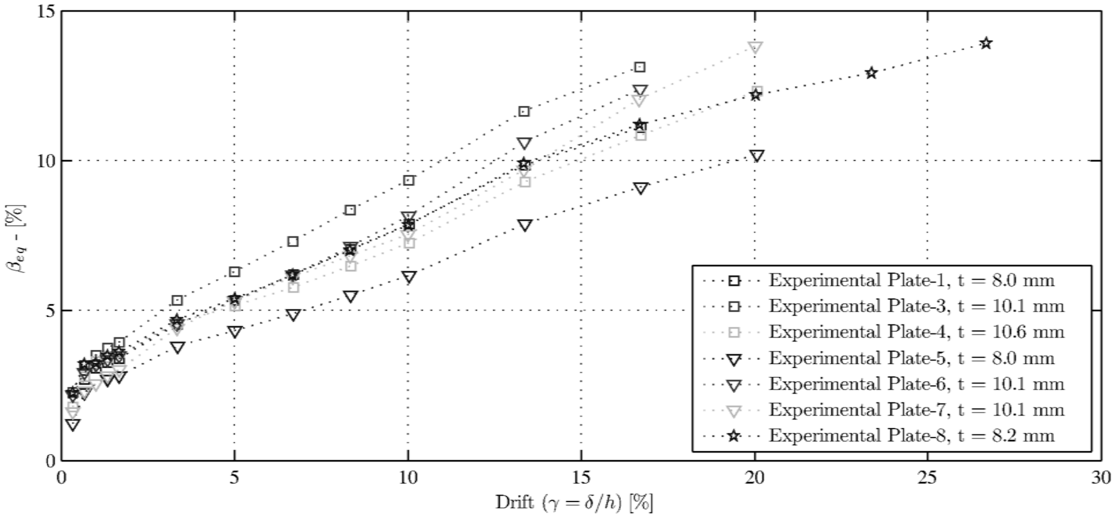

Fig. 11 Equivalent damping ratio as a function of drift

In order to analyze the fracture zone, a fractography was taken to one hourglass-shaped plate (Plate-7) and one tensile coupon (C-4), which are shown in Fig. 12. The plate grain size is about one third of the coupon grain size. Because the final thermal treatment was carried out for the same period of time for both types of elements, and coupons have less volume, the treatment induced more grain growth to these than to the plates. As mentioned in Somerday *et al*. (1997), this difference in grain size affects the post-yield stiffness.

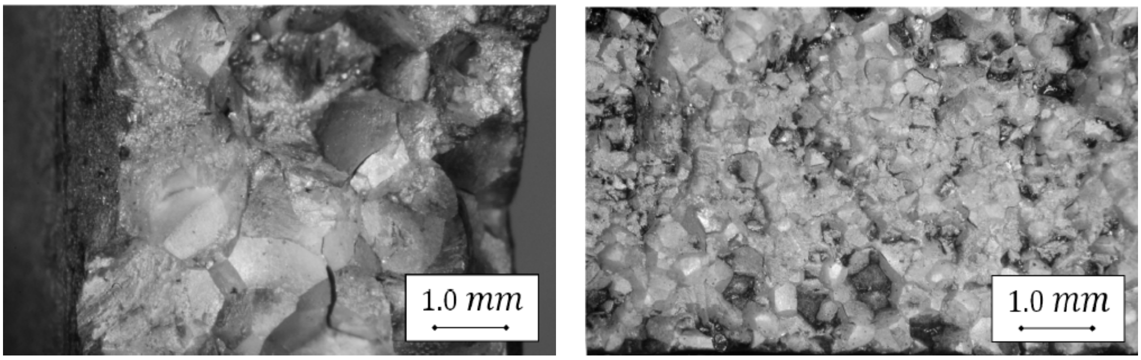

(a) Tensile coupon (C-4) (b) Hourglass-shaped plate (Plate-7)

Fig. 12 Specimen fractographies

3. Numerical study

3.1 Constitutive law model

The multilinear constitutive model for SMA proposed by Motahari and Ghassemieh (2007), shown in Fig. 13, was calibrated using the experimental data from the tensile coupon tests. The parameters of the model (σ_s^{cr}, σ_f^{cr}, E_m, and ε_L) were computed using the following procedure:

1. A linear regression was carried out to the initial points to determine the elastic properties, and the value of E_m was taken as the slope of the resulting line.
2. The post yielding stiffness was computed as the line that passes through the maximum tension point of the test and equates the areas under the envelopes of the test data and the model.
3. For each heat, a value ε_L was selected iteratively in such a way that the unloading curve passes through that point, and the maximum strain attained in tests should be below the point where hardening could occur (σ_f^{cr}).
4. The intersection of the post yielding stiffness with the initial line gives σ_s^{cr} and with the unloading curve gives σ_f^{cr}.

The resulting parameters are summarized in Table 4. Heat B presents larger average elastic module E_m and transformation stress σ_s^{cr} than Heat A, and all the parameters have a high variability. This means that at this stage of the research, tensile tests must be performed in order to obtain the proper constitutive law model. Fig. 14 shows the experimental and numerical results. The numerical model presents an adequate correlation with the experimental results, although slightly underpredicting the maximum stress at each intermediate cycle. One of the limitations of the model is the constant slope of the unloading path, which does not represent the actual unloading path of the material. This affects the energy loss (E_d), because the model dissipates more energy (more area in the cycle) than the experiment.

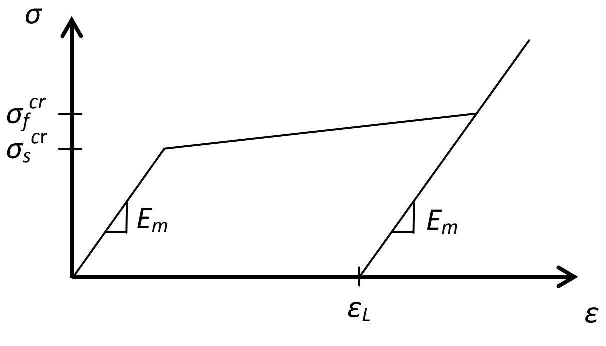

Fig. 13 Model proposed by Motahari and Ghassemieh (2007)

Table 4 Parameters for constitutive model

Coupon	Heat	E_m [GPa]	σ_s^{cr} [MPa]	σ_f^{cr} [MPa]	ε_L [%]
C-1	A	51.60	170.1	319.2	2.0
C-3	A	47.73	175.0	382.8	2.0
C-4	B	60.64	257.0	477.9	4.0
C-5	B	62.40	268.5	475.4	4.0
C-6	B	48.39	257.2	394.9	4.0
C-7	B	48.95	253.1	427.0	4.0
C-8	B	56.84	258.9	495.0	4.0

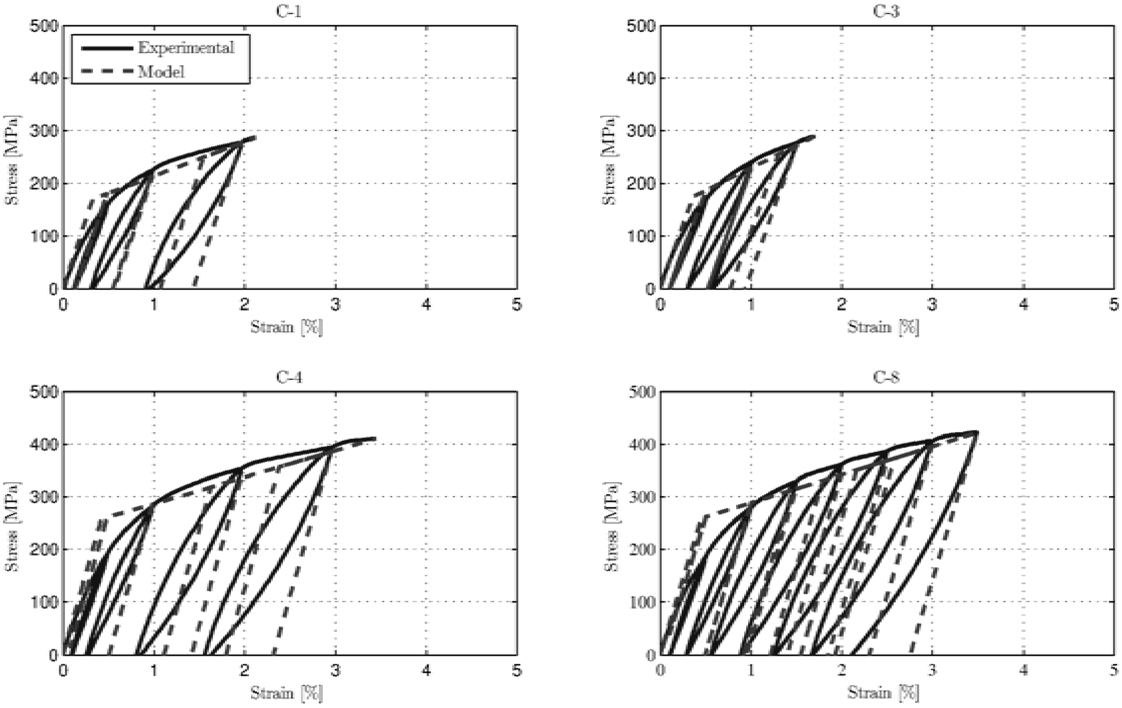

Fig. 14 Comparison between experimental and analytical constitutive law

3.2 Plate model

A finite element model, which predicts the flexural behavior of the plates, was developed to be used for preliminary design of hourglass-shaped plates. The software MATLAB (2009) is used as computational framework. The plate was divided in 16 segments along the length. Each segment had a constant width (equal to the average width of the segment) and it was represented by 10 uniaxial fibers (see Fig. 15). The stress-strain behavior of each fiber was modeled with the non-linear constitutive law, previously obtained in section 3.1.

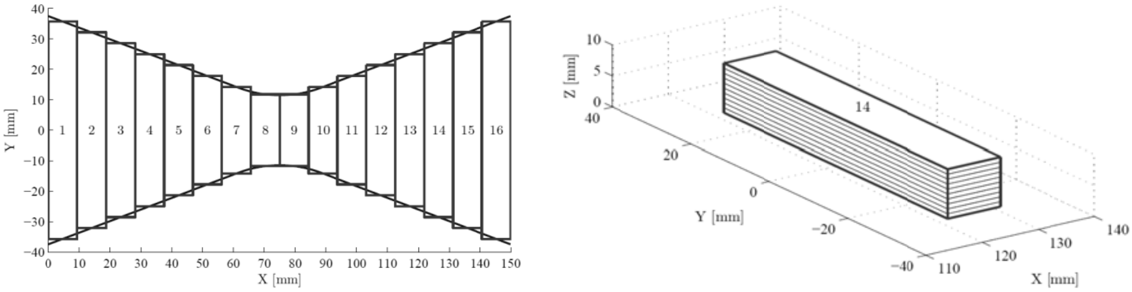

(a) Discretization along the plate length.

(b) Discretization of the cross section

Fig. 15 Schematic plate model

Typical energy dissipation devices for civil structures include a number of hourglass-shaped plates acting in parallel. This configuration induces the same displacement to every plate. The proposed model can be used with different material models (e.g., martensite with shape memory effect, austenite with superelastic effect, copper, steel, etc) and plate geometries. The force on the plate can then be multiplied by the number of equal plates. The summation of all the plate forces is the force of the entire device at each step, which, in addition to the displacement history, can be used in large complex structural models. This is useful for the design phase of these devices, where different configurations (number, geometry and material of plates) that might have more or less energy dissipation and/or self-centering capacity, can be studied to select the most appropriate.

In this work, only one plate was modeled (as experimented), with the measured geometry of each tested element. The stress-strain relationship of the fibers was modeled using the parameters determined from the coupon tests, but with a modification to the constitutive law: the parameter σ_f^{cr} was multiplied by 2.5, in order to increase the second slope of the constitutive law model. This change was justified by the significant difference between the grain size of plates and coupons (see Fig. 12). Fig. 16 shows the experimental and analytical force-displacement curves obtained for Plate-8. As can be seen, the global behavior of the plates is correctly reproduced by the model.

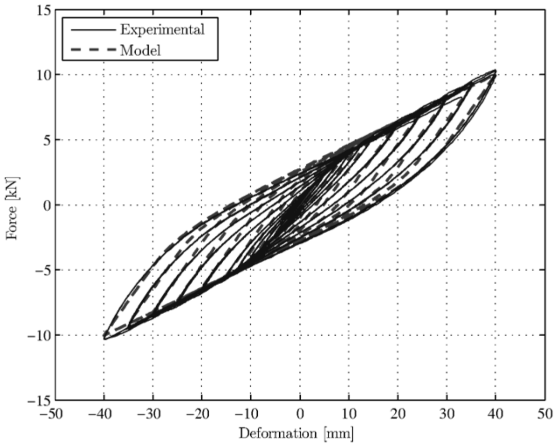

Fig. 16 Comparison between experimental and analytical force-displacement curves

Effective normalized stiffness and energy loss were computed for each cycle, as it was done for experimental data. These results are included in Figs. 9 and 10. The model can predict the effective stiffness and energy loss with mean differences of 3.4% and 54.4%, respectively. While stiffness is properly predicted by the model, the significant difference for the energy loss is mainly due to the unloading slope limitation of the constitutive law model, as stated in section 3.1. The equivalent damping ratio was not computed for the model, as it does not affect the design of these devices, and it is only used to compare the efficiency of different energy dissipation systems.

Theoretical expressions for the yielding point and elastic stiffness can be obtained from an elastic analysis of the hourglass-shaped plates (Eqs. (3) and (4)).

$$K_{el} \approx 0.775 \frac{E_m B t^3}{h^3} \tag{3}$$

$$F_y = \frac{\sigma_s^{cr} B t^2}{3h} \tag{4}$$

Where B, h, and t are the geometric properties of the hourglass-shaped plate (width at the ends, length, and thickness respectively). In addition, K_{el} and F_y were computed for both the experimental and numerical curves using a bi-linearization of the envelope curve. The results are shown in Figs. 17 and 18. Mean differences of 2.7% and 5.0% where found between the finite element model and experimental K_{el} and F_y, respectively. The theoretical equations predictions for these parameters, shown above, had mean differences of 3.6% and 13.9% with the experimental values. In general, Heat A plates (Plate-1 and Plate-3) have a lower elastic stiffness and yielding force than Heat B plates of similar thickness, which is consistent with the tension tests results.

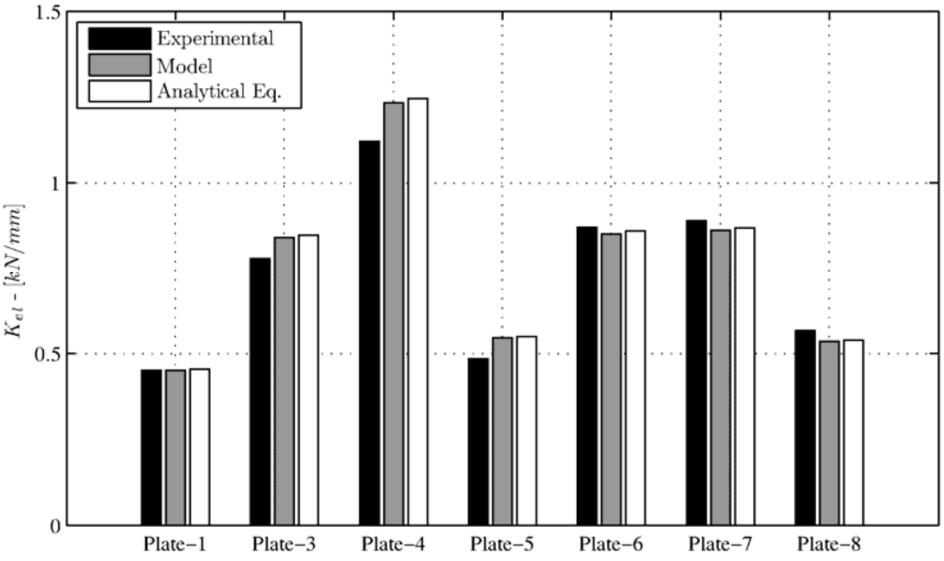

Fig. 17 Elastic stiffness of each specimen

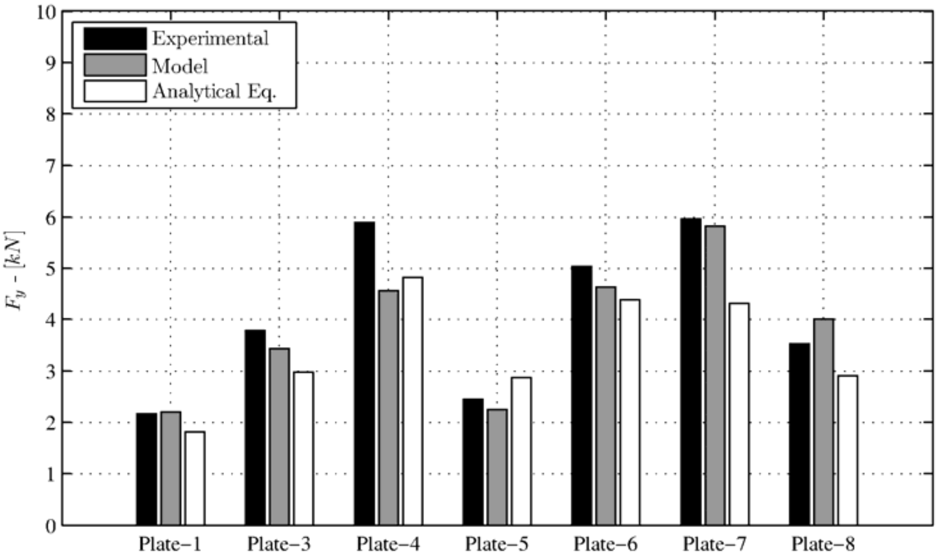

Fig. 18 Yielding force of each specimen

4. Conclusions

Hourglass-shaped plates were fabricated using two CuZnAl alloys and tested under cyclic transverse flexure to study their potential as a seismic energy dissipation device. In addition, cyclic tension tests on material coupons were conducted to capture the material's constitutive law. A numerical study was conducted to predict the behaviour of the plates. The following major conclusions can be drawn:

- Heat A is slightly less ductile than Heat B and both are in martensite phase at room temperature.
- No dependency on the excitation frequency (between 0.025 and 1 [Hz]) was observed on tensile tests.
- Plates dissipate energy through repeatable stable hysteresis cycles without strength degradation. The behaviour is nonlinear and depends on the displacement amplitude: effective stiffness decreases with increasing amplitudes and tends to stabilize at around 40-50% of the original value, while energy loss and equivalent damping ratio increase with increasing amplitudes. The equivalent damping ratio reaches values of up to 13%, comparable with other energy dissipation devices.
- The model used for the constitutive law of the material adequately captures the experimental strain-stress behaviour, even though the detwinning process was not completed.
- Generic values of each parameter of the constitutive law model could not be obtained. Tensile tests must be conducted in order to use proper parameters in the plate model.
- The proposed nonlinear plate model can be used to predict the plate global behaviour and properties (maximum force, effective stiffness, energy loss, yielding point).

- A comparison between theoretical expressions and experimental results for yielding point and elastic stiffness shows mean differences of 3.6% and 13.9%, respectively. This validates the use of simple analytical expressions as first approximation in design of these types of seismic dissipation devices.

The alloy used in this research it is not yet in a stage where fabrication can warrant reproducible properties, therefore further work is required in this area. Furthermore, the effect of aging and training of the material on its superelastic and/or shape memory characteristics, as well as its fatigue life, need also be studied.

Acknowledgements

The authors gratefully acknowledge the financial support of CONICYT, Chile, through FONDECYT project 1070370. The first author acknowledges the financial support from CONICYT Fellowships for Graduate Studies Program. The work conducted at Georgia Institute of Technology was possible thanks to the funding provided by the Program for Short Research Stays of the Department of Graduate Studies, University of Chile, and the important contribution of Professor Reginald DesRoches and Chuang-Sheng Yang at Georgia Institute of Technology.

References

Abdulridha, A., Palermo, D., Foo, S. and Vecchio, F.J. (2013), “Behavior and modeling of superelasticshape memory alloy reinforced concrete beams”, *Eng. Struct.*, **49**, 893-904.

Alam, M.S., Moni, M. and Tesfamariam, S. (2012), “Seismic overstrength and ductility of concrete buildings reinforced with superelastic shape memory alloy rebar”, *Eng. Struct.*, **34**, 8-20.

Alonso, J. (1989), *Mechanical characteristics of X-Plate energy dissipators*, CE-299 REPORT, College of Engineering, University of California, Berkeley.

Asgarian, B. and Moradi, S. (2011), “Seismic response of steel braced frames with shape memory alloy braces”, *J. Constr. Steel Res.*, **67**(1), 65-74.

Beltran, J.F., Cruz, C., Herrera, R. and Moroni, M.O. (2011), “Shape memory alloy CuAlBe strands subjected to cyclic axial loads”, *Eng. Struct.*, **33**(10), 2910–2918.

Bhuiyan, A.R. and Alam, M.S. (2013), “Seismic performance assessment of highway bridges equipped with superelastic shape memory alloy-based laminated rubber isolation bearing”, *Eng. Struct.*, **49**, 396-407.

Carreras, G., Casciati, F., Casciati, S., Isalgue, A., Marzi, A. and Torra, V. (2011), “Fatigue laboratory tests toward the design of SMA portico-braces”, *Smart Struct. Syst.*, **7**(1), 41-57.

Casciati, S., and Marzi, A. (2010), “Experimental studies on the fatigue life of shape memory alloy bars”, *Smart Struct. Syst.*, **6**(1), 73-85

Casciati, F. and Van der Eijk, C. (2008), “Variability in mechanical properties and microstructure characterization of CuAlBe shape memory alloys for vibration mitigation”, *Smart Struct. Syst.*, **4**(2), 103-121.

De la Llera, J.C., Esguerra, C., Almazán J.L. (2004), “Earthquake behavior of structures with copper energy dissipators”, *Earthq. Eng. Struct. D.*, **33**(3), 329-358.

Dieng, L., Helbert, G., Chirani, S.A., Lecompte, T. and Pilvin, P. (2013), “Use of shape memory alloys damper device to mitigate vibration amplitudes of bridge cables”, *Eng. Struct.*, **56**, 1547-1556.

Dong, J., Cai, C.S. and Okeil, A.M. (2011), “Overview of potential and existing applications of shape memory alloys in bridges”, *J. Bridge Eng.*, **16**(2), 305-315.

Gibson, P. (2008), “Fabricación y caracterización de una aleación con memoria de forma CuZnAl considerada para disipadores sísmicos”, Mechanical Engineering Thesis (In Spanish), Universidad de Chile, Santiago, Chile.

Johnson, R., Padgett, J.E., Maragakis, M.E., DesRoches, R. and Saiidi, M.S. (2008), “Large scale testing of Nitinol shape memory alloy devices for retrofitting of bridges”, *Smart Mater. Struct.*, **17**(3), art.no. 035018.

MATLAB (2009), Version 7.8.0.347 (R2009a), February, www.mathworks.com

McCormick, J.P. (2006),“Cyclic behavior of shape memory alloys: Material characterization and optimization”, Ph.D. Dissertation, School of Civil and Environmental Engineering, Georgia Institute of Technology, Atlanta.

Miller, D.J., Fahnestock, L.A. and Eatherton, M.R. (2012), “Development and experimental validation of a nickel–titanium shape memory alloy self-centering buckling-restrained brace”, *Eng. Struct.*, **40**, 288-298.

Montecinos, S., Cuniberti, A. and Sepúlveda, A. (2008),“Grain size and pseudoelastic behavior of a Cu-Al-Be alloy”, *Mater. Charact.*, **59**(2),117-123.

Motahari, S.A. and Ghassemieh, M. (2007), “Multilinear one-dimensional shape memory material model for use in structural engineering applications”, *Eng. Struct,*, **29**(6), 904-913.

Somerday, M., Wert, J.A. and Comstock, R.J, (1997),“Effect of grain size on the observed pseudoelastic behavior of a Cu-Zn-Al shape memory alloy”, *Metall. Mater. Trans. - A*, **28**(11), 2335-2341.

Speicher, M.S., DesRoches, R. and Leon, R.T. (2011), “Experimental results of a NiTi shape memory alloy (SMA)-based recentering beam-column connection”, *Eng. Struct.*, **33**, 2448-2457.

Sutou, Y., Omori, T., Yamauchi, K., Ono, N.,Kainuma, R. and Ishida, K. (2005),“Effect of grain size and texture on pseudoelasticity in Cu-Al-Mn-based shape memory wire”, *Acta Materialia*, **53**(15), 4121-4133.

Symans, M.D., Charney, F.A., Whittaker, A.S., Constantinou, M.C., Kircher, C.A., Johnson, M. W. and McNamara, R.J. (2008), “Energy dissipation systems for seismic applications: Current practice and recent developments”, *J. Struct. Eng. – ASCE*, **134**(1), 3-21.

Tena-Colunga, A. (1997), “Mathematical modelling of the ADAS energy dissipation device”, *Eng. Struct.*, **19**(10), 811-821.

Torra, V., Auguet, C., Isalgue, A., Carreras, G., Terriault, P. and Lovey, F.C. (2013),“Built in dampers for stayed cables in bridges via SMA. The SMARTeR-ESF project: A mesoscopic and macroscopic experimental analysis with numerical simulations”, *Eng. Struct.*, **49**, 43-57.

Vargas, J. (2007), *Ensayo de placas tipo ADAS de láminas de CuZnAl*, Civil EngineeringThesis (In Spanish), Universidad de Chile, Santiago, Chile.

Youssef, M.A., Alam, M.S. and Nehdi M. (2007), “Experimental investigation on the seismic behavior of beam-column joints reinforced with superelastic shape memory alloys”, *Earthq. Eng.*, **12**(7), 1205-1222.

FC